Thermocapillary Flows in a Rotating Float Zone Under Microgravity

A Galerkin finite-element method is used to study the steady rotating, thermocapillary fluid flow in the cylindrical float zone configuration for crystal growth. Results are presented for a fluid of Prandtl number 1.0 in a zone of unit aspect ratio under microgravity conditions. In the absence of rotation, the thermocapillary flow is responsible for large radial nonuniformities in the heat transfer, especially at the cold boundary. A sufficiently strong uniform corotation of the end rods leads to a rigid rotation of the fluid in the interior of the zone; in this case, the thermocapillary flows are considerably attenuated and confined to a region near the free surface of the zone. This provides a more uniform thermal environment over the bulk of the crystal-melt boundary, which is a very desirable processing condition. When the end rods are counterrotated, inertially driven meridional flow cells appear in the zone. The interaction of the rotational forced convection with the thermocapillary flow causes the region of the local heat transfer minimum at the cold boundary to gradually shift away from the axis of the zone toward the meniscus.

Ramesh Natarajan
Department of Chemical Engineering
Massachusetts Institute of Technology
Cambridge, MA 02139

Introduction

In recent years there has been considerable interest in exploiting the microgravity environment on board orbiting spacecraft for the processing and purification of crystalline materials (Carruthers and Testardi, 1983). The absence of large gravitational forces makes the use of containerless technologies feasible and this enables the processing of high-purity materials without fear of contamination from the container walls. In addition, the microgravity environment is of particular interest in crystal growth applications because of the possibility of suppressing the complicated, and often turbulent, buoyancy-driven flows that occur in crystal melts during thermal processing. The presence of such flows makes it difficult to precisely control the thermal boundary conditions at the melt-crystal interface; this leads to variations in the rates of solidification and solute impurity retention at the phase boundary. The deleterious effects of melt flows on product quality have been experimentally observed by Kim et al. (1972) in a model Czochralski crystal growth configuration.

Chun (1980) and Priesser et al. (1983) have conducted experiments in model small-scale float zones that simulate the effect of the microgravity environment on the melt flows in crystal growth processing applications. Thermal buoyancy flows are generally negligible in the subcentimeter-size zones used in these experiments; however, a substantial bulk convection can still arise due to the surface shear stresses that are generated through the temperature-dependent variations in the surface tension at the exposed surfaces of the melt. The understanding and control of these so-called thermocapillary flows is thus important in evaluating the potential for microgravity-based materials processing applications.

In the model experiments, a cylindrical float zone is typically formed between two highly conducting circular end rods. The use of an optically transparent fluid in the zone facilitates visual observation of the flow. Thermocapillary flows are generated either by maintaining a fixed temperature difference across the two end rods or through the temperature gradients due to the radiant heat flux from a circumferentially mounted heater. The nature and intensity of the resulting thermocapillary flow depends on the experimental geometry and on the magnitude of the temperature gradients along the melt free surface. The dependence on the temperature gradient can be characterized in terms of the Marangoni number, defined in the Problem Formulation section. The experimental observations indicate that if the boundary conditions are axisymmetric and time-independent, then at low Marangoni numbers the flow in the zone is also steady and axisymmetric. At somewhat larger Marangoni num-

The author's current address is P.O. Box 704, IBM T. J. Watson Center, Yorktown Heights, NY 10598

bers, the steady flows are unstable to nonaxisymmetric perturbations, leading to a wavelike flow of constant frequency propagating in the azimuthal direction. The critical Marangoni numbers at the onset of this time-dependent flow instability have been experimentally measured; however, the interactions that are responsible for this interesting phenomenon are not completely understood.

Priesser et al. (1983) used molten sodium nitrate (Prandtl number 8.9) as the zone liquid in their experiments. The effect of thermal buoyancy convection was minimized by using a sufficiently small zone and by imposing a gravitationally stable vertical temperature gradient across the end rods. The dominance of thermocapillary convection in such zones was visually confirmed by forming a viscous film on the zone surface to suppress the surface tension gradients, whereupon the flows were found to be considerably diminished in strength. However, even in their carefully chosen experimental configuration, weak thermal buoyancy flows could still arise from the radial temperature gradients in the zone. These were especially visible near the axis of zones of small aspect ratio, in which the thermocapillary flows are basically confined to a region near the meniscus. Their experiments also showed that the onset of the nonaxisymmetric, wavelike instabilities occurred at a critical Marangoni number of about 10^4, with the exact critical value and the spatial form and frequency of the unstable mode depending on the zone aspect ratio.

The feed and product rods are often rotated in commercial float zone processing applications in order to smooth out azimuthal variations in the external thermal conditions. This rotation also leads to a forced convection in the liquid melt which interacts with the thermocapillary flows that are simultaneously present. Chun (1980), conducted experiments with a silicone oil (Prandtl number 7.1) and studied the effect of various end-rod rotation strategies, ranging from equal corotation to equal counterrotation, on the flow fields within the float zone. A notable feature of these experiments is the indication that a small amount of end-rod rotation can stabilize the axisymmetric thermocapillary flows by damping out the instability modes (see also Chun and Wuest, 1982). The reasons for this phenomenon are also not well understood at this time.

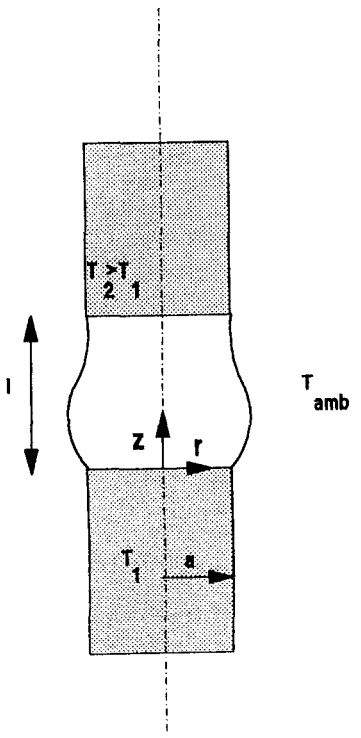

Figure 1. Idealized float zone.

The present investigation is concerned with the nature of the steady axisymmetric flows that arise in small-scale zones under microgravity conditions. The emphasis is on computing accurate representations of the basic flow field. The work is directed toward an eventual quantitative understanding of the mechanism for the onset of time-dependent and transitional flows in small-scale float zones. While such a quantitative understanding is of fundamental interest, it is also useful in devising process control strategies for crystal growth applications and in providing accurate predictive models for the processing of new materials with existing technologies. An example of the utility of such a modeling approach is already provided by the fact that the optically transparent liquids used in the flow visualization experiments have fairly high Prandtl numbers. The extension of the experimental results to the very low Prandtl numbers (characteristic of metallic alloys and semiconductors) that are of interest in realistic float zone processing applications requires careful justification.

Problem Formulation

Consider a float zone of radius a and length l as shown in Figure 1. The fluid in the zone has a viscosity μ, kinematic viscosity ν, thermal conductivity k, thermal diffusivity κ, and its density ρ and surface tension σ are assumed to vary linearly with temperature in the form

$$\rho = \rho_0[1 - \alpha(T - T_0)] \tag{1}$$

$$\sigma = \sigma_0 - \gamma(T - T_0) \tag{2}$$

where ρ_0 and σ_0 are the values of the density and surface tension at some arbitrarily chosen reference temperature T_0. The temperatures of the two end rods are given by T_1 and T_2 (with $T_2 > T_1$) and their angular velocities are $s\hat{\Omega}$ and $\hat{\Omega}$, respectively. The heat transfer coefficient at the melt free surface is given by h.

The following scales are chosen to nondimensionalize the governing equations: length a, velocity $\gamma(T_2 - T_1)/\mu$, pressure $\gamma(T_2 - T_1)/a$, and temperature $T_2 - T_1$. The insertion of these scalings into the relevant field equations leads to the appearance of various dimensionless quantities, which are defined below. The magnitudes of these quantities will determine the simplifying approximations to the governing equations that are appropriate to our present study. The relevant quantities are

Reynolds number,

$$Re = \frac{\gamma(T_2 - T_1)a}{\mu\nu}$$

Prandtl number,

$$Pr = \frac{\nu}{\kappa}$$

Dynamic bond number,

$$R = \frac{\rho \alpha g a^2}{\gamma}$$

Aspect ratio,

$$As = \frac{a}{l}$$

Biot number,

$$Bi = ha/k$$

Rotation number,

$$\Omega = \frac{\hat{\Omega} a \mu}{\gamma (T_2 - T_1)}$$

Gravitational Bond number,

$$Bo_g = \frac{\rho g a^2}{\sigma}$$

Capillary number,

$$Ca = \frac{\gamma (T_2 - T_1)}{\sigma}$$

In addition, results are frequently expressed in terms of the derived quantity,

Marangoni number,

$$Ma = PrRe$$

The magnitudes of these various quantities can be estimated as follows. We consider a zone of radius 0.3 cm and unit aspect ratio. Using the material properties of a silicon melt (Pr = 0.023; see Table 1 of Smith, 1986, for other reference values) and a moderately large value for the characteristic temperature gradients in the zone, say 2 K/cm, we estimate $Re \approx 3{,}000$ and $Ca \approx 10^{-4}$. Under microgravity conditions, R and Bo_g will be negligibly small, but in normal gravity for such zones we find that $R \approx 0.07$ and $Bo_g \approx 0.3$. For these temperature gradients, the value of Ω is about 0.2 for a zone that is rotated at about 20 rev/s.

In estimating these dimensionless quantities we have chosen a velocity scaling that reflects the thermocapillary nature of the basic flow. In this paper we are also interested the case when the end rods are uniformly rotated (i.e., $s = 1$) at a very large angular velocity, where it is perhaps more appropriate to use a scaling that reflects the rotational aspect of the flow. This scaling leads to the following dimensionless quantities

Ekman number,

$$E = \frac{\nu}{\hat{\Omega} a^2}$$

Rossby number,

$$Ro = \frac{\gamma (T_2 - T_1)}{\hat{\Omega} a \mu} = \frac{1}{\Omega}$$

Rotational Bond number,

$$Bo_r = \frac{\rho \hat{\Omega}^2 a^3}{\sigma}$$

Buoyancy number,

$$B = \frac{\beta \hat{\Omega} a \mu}{\gamma}$$

and using the same characteristic values for the various quantities as in the previous paragraph, we estimate $E \approx 0.002$, $Ro \approx 4$, $Bo_r \approx 0.04$, and $B \approx 10^{-5}$.

One of the primary difficulties in this problem is the determination of the shape of the zone meniscus. In the absence of all fluid flow—that is, in a static zone with no imposed temperature gradients—the shape of the meniscus is determined by three factors: by the contact angle condition at the meniscus-rod boundary, by gravity, and by the centrifugal pressure due to any rigid rotation of the fluid in the zone. In order to simplify the analysis, we assume in the present instance that the contact angle is 90° and that the gravitational and rotational Bond numbers, Bo_g and Bo_r, are negligibly small. The contact angle assumption is justified for experimental configurations that were discussed in the Introduction. The magnitude of Bo_g is small under microgravity conditions but not necessarily so in a normal gravity experiment. Likewise, the magnitude of Bo_r is negligibly small in slowly rotating, small-scale zones. In any event, under these assumptions the equilibrium meniscus shape can be taken to be cylindrical. In the nonstatic case—that is, when there is fluid flow in the zone—dynamical normal stresses are exerted on the meniscus. In addition, spatial variations in the capillary pressure also arise from the temperature dependence of the surface tension. These two effects however, are scaled by the capillary number Ca, which is negligibly small in the present instance. The free boundary condition that determines the shape of the zone meniscus is the well-known Young-Laplace equation, which gives the jump in pressure across the free surface as the product of the surface tension and mean interfacial curvature. Under the assumptions made on the magnitudes of the various dimensionless parameters Bo_r, Bo_g, and Ca, and on the meniscus-rod contact angles, this boundary condition may be dropped and the meniscus shape assumed to be a cylinder on which the normal component of the fluid velocity vanishes.

The relevant equations governing the steady, axisymmetric fluid flow and heat transfer in a zone of unit aspect ratio are then given by

$$Re\, v \cdot \nabla v = -\nabla p + \nabla \cdot \tau \tag{3}$$

$$\nabla \cdot v = 0; \quad \tau = \nabla v + (\nabla v)^T \tag{4}$$

$$Ma\, v \cdot \nabla T = \nabla^2 T \tag{5}$$

along with the boundary conditions

$$\text{at } z = 0; \quad T = 0, v = s\Omega r e_\theta \tag{6}$$

$$\text{at } z = 1; \quad T = 1, v = \Omega r e_\theta \tag{7}$$

$$\text{at } r = 1; \quad v \cdot e_r = 0,$$

$$-\frac{\partial T}{\partial r} = Bi[T - T_{amb}(z)], \tau_{rz} = -\frac{\partial T}{\partial z} \tag{8}$$

where T_{amb} is the ambient temperature. Note that the field equations have been simplified by neglecting all effects that arise when gravity is significant. Hence, the present analysis is valid only under microgravity conditions.

The dimensionless Nusselt numbers Nu_1 and Nu_2 give the total heat flux to the two end rods and are defined as

$$Nu_1 = \int_0^1 -\left.\frac{\partial T}{\partial z}\right|_{z=0} r\,dr,$$

$$Nu_2 = \int_0^1 -\left.\frac{\partial T}{\partial z}\right|_{z=1} r\,dr \tag{9}$$

respectively. We note that in the absence of any heat flux through the sides of the zone, that is, when $Bi = 0$, the sum of these two quantities must be zero.

Previous Related Work

Kobayashi and Wilcox (1982) considered the effect of the forced convection due to end-rod rotation on the temperature field within the zone. The numerical computations were carried out for $Re = Ra = 0$; that is, thermocapillary and thermal bouyancy flow effects were neglected in the analysis. Thus, in the absence of end-rod rotation, the temperature field in the zone was simply the conduction profile due to the external heating boundary conditions. The flow field due to end-rod rotation can be independently determined from the Navier-Stokes equations. This flow affects the temperature field through the convective terms in the energy equation, Eq. 5. These convective terms are scaled by the Prandtl number, so that their results showed, as expected, that at low Prandtl numbers the temperature field is practically independent of the flow field. Murthy (1987) has extended these calculations to higher rotational velocities as well as to the consideration of the distribution of a passive solute.

Kobayashi (1984) has considered the interaction of thermocapillary and end-rod-rotation driven flows at moderately large values of Re and with $E = 0.01$. Various end-rod rotation strategies were considered, including corotation ($s = 1$), single-rod rotation ($s = 0$), and counterrotation ($s = -1$). Kobayashi's definition of the Reynolds number is based on the heat flux due to a circumferential heater and thus differs from the definition used in the present work, which is based on the temperature difference between the end rods. The calculations presented here extend Kobayashi's work to the consideration of a new heating geometry as well as to a parametric range where rotational and thermocapillary effects are pronounced.

Harriott and Brown (1983) have considered the flow field in an isothermal float zone due to end-rod rotation. The Reynolds number appropriate to the isothermal problem studied by them is the inverse of the Ekman number as defined in the previous section. They obtain an analytical solution to the flow field through an asymptotic expansion method that is valid for small Reynolds numbers. These results have been numerically extended to larger values of the Reynolds number in Harriott and Brown (1984). These computations show that inertial effects can lead to multiple steady solutions for the flow when the Reynolds number is greater than about 100.

Smith (1986) has considered the thermocapillary flow in a uniform, rapidly rotated float zone. The governing equations were considered in a frame of reference rotating uniformly with the end rods. The assumption that the Rossby number $Ro \ll 1$, enables the nonlinear inertial terms to be neglected from the analysis. A boundary layer analysis of the resulting linear equations, valid for small values of E, shows that the flow field in the interior of the zone is inviscid and in a state of rigid rotation with the end rods. This is a manifestation of the Taylor-Proudman theorem for slow, inviscid rotating fluid flows. The thermocapillary flow is confined to a viscous boundary layer near the zone meniscus of thickness $O(E^{1/3})$. In addition, there are Ekman layers of thickness $O(E^{1/2})$ located within the viscous side layer at the surfaces of the end rods which permit the azimuthal velocities in the side layer to be matched to the end-rod boundary conditions. Smith's analysis shows that, to leading order for a small Ekman number, the flow and temperature distribution in the zone interior is independent of the flow in the viscous boundary layers at the meniscus.

This problem was reconsidered by Fowlis and Roberts (1986) using a different boundary condition for the temperature variation at the meniscus boundary. A linear, noninertial, boundary layer analysis similar to that carried out by Smith was compared with numerical solutions of the full field equations. Their results indicate that as the temperature driving force for the thermocapillary flow is increased at a fixed uniform rotation rate, these flows cannot be confined to the meniscus region as predicted by the linear theory. Fowlis and Roberts however point out that this may be due to the fixed temperature boundary condition used in their model, which leads to an overestimate for the magnitude of the thermocapillary flows, even at the small values of the Prandtl number ($Pr = 0.023$) used in their computations. These conclusions are complementary to the results obtained in this paper, where we show that at larger Prandtl numbers, the self-modification of the temperature gradients at the boundary due to the flow leads to relatively strong rotational confinement effects, even when the Marangoni number is very large.

Rybicki and Floryan (1987) consider the thermocapillary flow in a cylindrical float zone with the field equations being linearized by neglecting the nonlinear advection terms in the field equations. In this case, the temperature field in the interior of the melt is given by the conduction equation, which is solved analytically for an arbitrarily specified external heat flux to the zone. The resulting temperature gradients are used to compute the Marangoni surface stresses, which provide the boundary conditions required to solve the Stokes equations for the flow field. These results are useful in interpreting the geometric features of the flow field for a variety of external heating conditions.

The work of Zebib et al. (1985) concerning the thermocapillary flow of a fluid with $Pr = 1$ in an open square cavity heated

from the side, is also of interest in the present context. Their numerical solutions show that at large Marangoni numbers a boundary layer regime is approached in which the flow in the cavity consists of an inner isothermal core of constant vorticity. The temperature gradients occur in viscous boundary layers of thickness $O(Ma^{-1/3})$ at the free surface, of thickness $O(Ma^{-1/2})$ at the side and bottom walls and in a viscous corner region of thickness $O(Ma^{-2/3})$ located within the free surface boundary layer at the cold wall. Aside from the obvious differences in geometry, similar results are obtained for the nonrotating thermocapillary flows studied in this paper.

Solution Method

The numerical solution of Eqs. 3–8 is obtained using a primitive variable Galerkin finite-element method (Thomasset, 1981). The flow domain is discretized into 9-node quadrangular, isoparametric finite elements on which the pressure, velocity, and temperature fields are expanded in the form

$$p = \sum_{i=1}^{M} p_i \chi_i(r, z) \tag{10}$$

$$\begin{bmatrix} u \\ v \\ w \end{bmatrix} = \sum_{i=1}^{N} \begin{bmatrix} u_i \\ v_i \\ w_i \end{bmatrix} \Phi_i(r, z) \tag{11}$$

$$T = \sum_{i=1}^{N} T_i \Phi_i(r, z) \tag{12}$$

where (u, v, w) are respectively the radial, azimuthal, and axial components of the velocity field. The coefficients in these expansions are the unknown values at the nodal points of the finite-element mesh. The basis functions used in Eqs. 10–12 have local support; the set $\chi_i(r, z)$ consists of piecewise continuous bilinear polynomials, while the set $\Phi_i(r, z)$ consists of piecewise continuous biquadratic polynomials. The use of Galerkin's method followed by the usual integration by parts yields the set of $(M + 4N)$ equations

$$\int V(\nabla \cdot v)\chi_i \, dV = 0 \quad \text{for } i = 1, M \tag{13}$$

$$\int V[Re\, v \cdot \nabla v \Phi_i e_k - p\nabla \cdot (\Phi_i e_k) + \tau : \nabla(\Phi_i e_k)] \, dV + \int_S (p\Phi_i e_k - \tau \cdot \Phi_i e_k) \cdot n \, dS = 0 \quad \text{for } i = 1, N \text{ and } k = r, \theta, z \tag{14}$$

$$\int V(Ma\, v \cdot \nabla T \Phi_i + \nabla T \cdot \nabla \Phi_i) \, dV - \int_S \nabla T \cdot n \Phi_i \, dS = 0 \quad \text{for } i = 1, N \tag{15}$$

where V and S denote the flow domain and its bounding surface respectively. The boundary conditions, Eqs. 6–8, are substituted into Eqs. 13–15 and the resulting set of nonlinear algebraic equations for the unknown nodal values solved iteratively using Newton's method. Each iteration step in Newton's method requires the solution of a linearized set of algebraic equations, which was carried out using the frontal elimination technique (Hood, 1976). The bulk of the computational work in the program is performed in the frontal routines, which have been efficiently vectorized. The program has also been optimized to minimize paging and it can therefore be used quite efficiently even on larger problems without excessive performance degradation.

The finite-element mesh used in the results reported here consists of 20 radial elements and 20 axial elements. This accuracy was found to be adequate for the present set of computations. The mesh was graded linearly toward the meniscus and toward the disk-rod boundaries in order to capture the sharp gradients expected near these boundaries. This discretization leads to a total of 7,165 equations for the unknown nodal variables with a front width of 194. The solution step at each Newton iterate required 56.4 s on a Cyber 205 computer with 4 million word memory and iterations were terminated when the relative error in the solution dropped below 2×10^{-5}.

The numerical results were visualized by plotting the con-

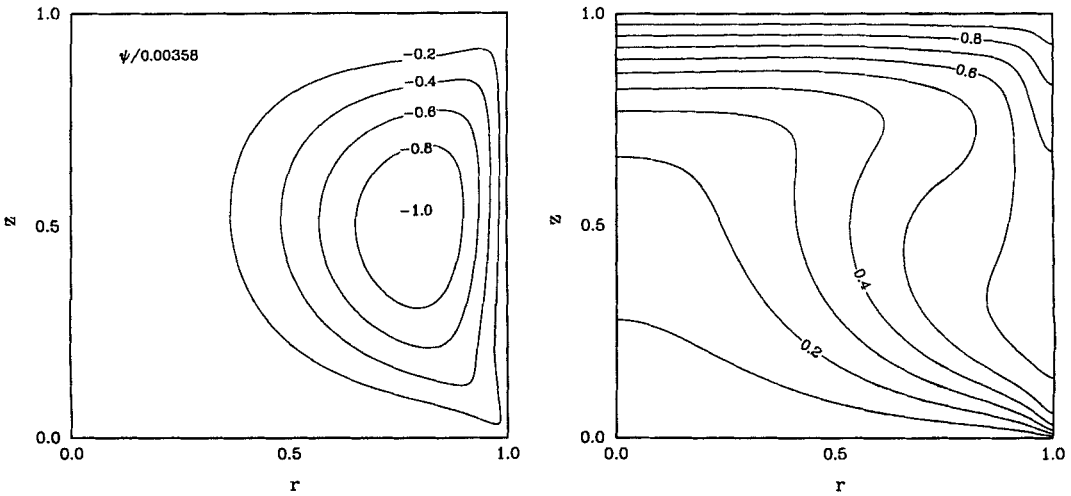

a. Streamlines b. Temperature Contours

Figure 2. Thermocapillary flow in a unit aspect ratio zone, with *Re* = 2,000.

tours of the temperature, the stream function of the meridional flows, and the azimuthal velocity. The stream function ψ was obtained from the converged solution for the velocity field by solving

$$\frac{\partial}{\partial r}\left(\frac{1}{r}\frac{\partial \psi}{\partial r}\right) + \frac{1}{r}\frac{\partial^2 \psi}{\partial z^2} = \frac{\partial u}{\partial z} - \frac{\partial w}{\partial r} \tag{16}$$

on the same finite-element mesh.

Numerical Results and Discussion

The calculations presented here cover three cases: the thermocapillary flow in the absence of any rotation of the end rods, and the effects of an equal corotation and an equal counterrotation of the end rods, respectively. These results are presented for a fluid of $Pr = 1$ in a zone of unit aspect ratio (i.e., $As = 1$) and an insulating boundary condition at the meniscus surface (i.e., $Bi = 0$).

No end-rod rotation

The streamlines and temperature contours obtained from the numerical solution are shown in Figure 2 for the case $Re = Ma = 2{,}000$. The cellular nature of the flow field is in good agreement with the experimental visual observations. The thermocapillary stresses along the meniscus drive a strong flow from the hot wall to the cold wall. A relatively weaker return flow is found in the zone interior. For the $Pr = 1$ fluid considered here, there is a strong coupling between the flow and temperature fields that leads to a considerable distortion of the temperature contours from the linear conduction profile.

The change in the nature of the flow field, especially at large Re, is illustrated by the variations of the axial velocity component at the meniscus surface, as shown in Figure 3. At low values of Re there are two relative maxima in the magnitude of the surface velocity. As Re increases, there is a substantial leveling of the surface velocity in the interior regions and the positions of the velocity maxima shift toward the end rods. In addition, the magnitude of the surface velocity in the interior regions decreases with increasing Re in an apparently paradoxical way. An explanation for this behavior is found in the surface temperature profile, since it is the gradient of the latter quantity that is basically responsible for driving the flow. In Figure 4 we see the development of a boundary layer axial temperature profile at the cold wall as Re is increased. The flattening of the temperature profile in the interior regions indicates that the driving force for producing large surface velocities will be small. In addition, the velocities that can be attained in the regions of the sharp temperature gradients are limited by the need to satisfy the velocity boundary condition at the end rods. The axial temperature profiles at the zone axis are also shown in Figure 4, which indicates the role of the return flow in modifying the temperature field. This effect is also seen in Figure 2, where the return flow is basically responsible for the sickle-shaped temperature contours seen in the interior of the zone.

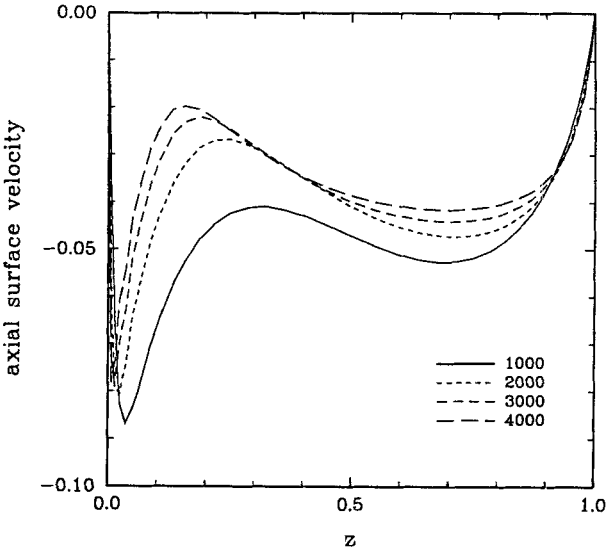

Figure 3. Surface velocity as a function of axial coordinate for various values of *Re*.

The differences in the gradients of the axial temperature profile at the end rods computed along the surface and along the zone axis, respectively, give some idea of the radial nonuniformities that result from the thermocapillary flow. This can also be

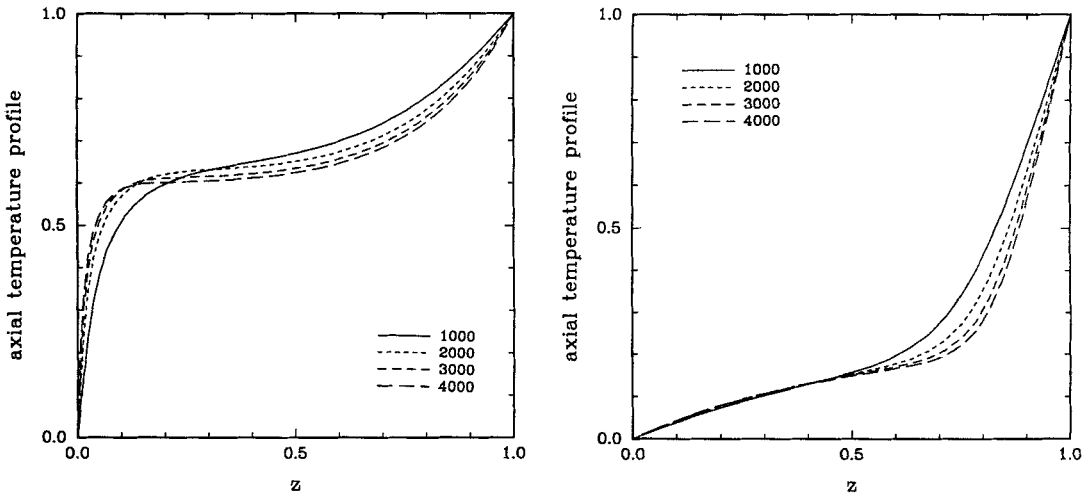

a. At Surface *b. At Zone Axis*

Figure 4. Axial temperature profiles for various values of *Re*.

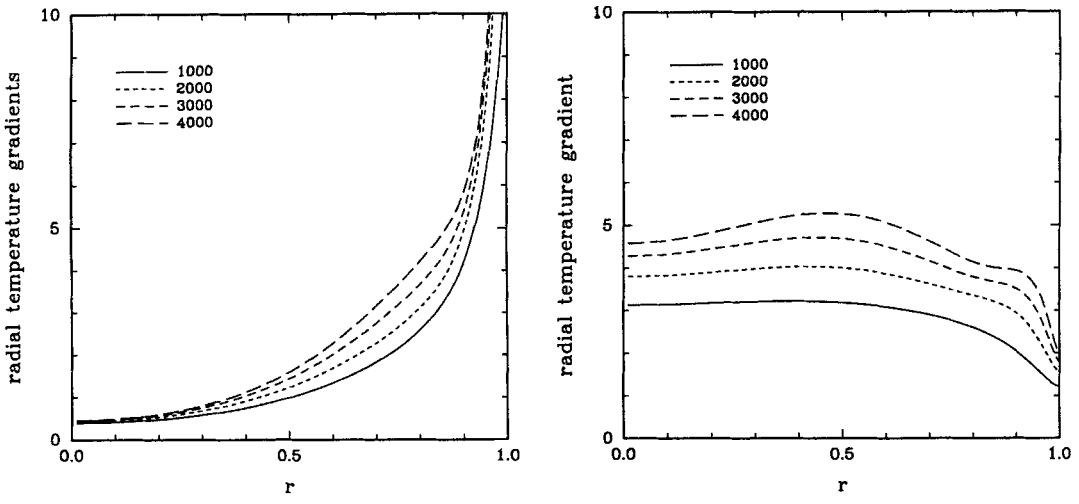

a. At Cold Wall *b. At Hot Wall*

Figure 5. Radial variations of axial temperature gradients for various values of *Re*.

seen in Figure 5, where these radial variations at the end rods are plotted in a more detailed way. The magnitude of the axial temperature gradient, or equivalently, the heat transfer at the cold boundary, increases sharply toward the meniscus. In the case $Re = 4{,}000$, the axial temperature gradients at the meniscus exceed that at the zone axis by a factor of about 90. In contrast, a much more uniform behavior is found at the hot boundary with the extreme magnitudes of this quantity differing by less than a factor of 5 across the cross section of the zone. These radial heat transfer variations have important consequences for crystal processing, where they lead to nonuniformities in the solidification rates and hence to a nonplanar crystal-melt growth boundary.

Zebib et al. (1985) have carried out a boundary layer scaling analysis for the thermocapillary flow in an open cavity, which is based on the hypothesis that at large *Re* the flow is driven primarily by the temperature variations in the interior portion of the meniscus rather than by the strong gradients in the boundary layer near the cold wall. Except for the obvious geometrical differences, there is good qualitative agreement between their observations and the results obtained here. In particular, the increase in *Nu* and the decrease in the magnitude of ψ_{min}, as shown in Table 1, are consistent with the boundary layer analysis although the present calculations have not been extended to the large Reynolds numbers that would enable a test of the predicted power law dependencies.

Table 1. Nusselt Numbers and Minimum Value of Axisymmetric Stream Function as a Function of Reynolds Number in a Zone with Unit Aspect Ratio

Re	Nu_1	Nu_2	$-\Psi_{min} \times 10^3$
1,000	−1.329	1.327	4.11
2,000	−1.721	1.708	3.58
3,000	−2.017	1.987	3.47
4,000	−2.266	2.214	3.38

Corotated end rods, $\Omega \neq 0$, $s = 1$

In the previous section, the results indicated that substantial flow velocities due to the return flow are found in the interior of the zone. In this section, we show that this flow pattern is considerably modified when the end rods are corotated at moderately large angular velocities.

The streamline contours in Figure 6 show that increasing the rotational velocity leads to the primary cell of the meridional

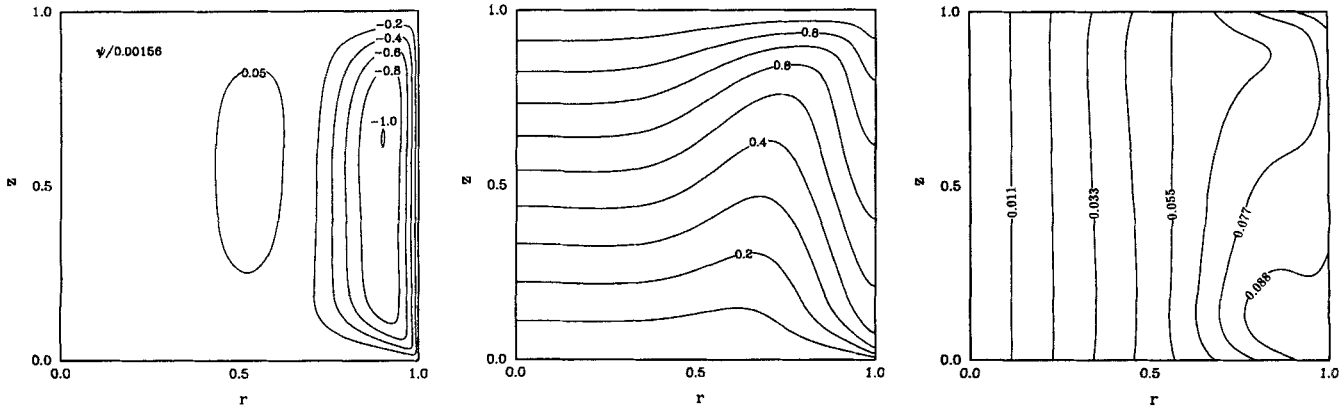

a. Streamlines of Meridional Flows *b. Temperature Contours* *c. Equally Spaced Angular Velocity Contours*

Figure 6. Equal end-rod corotation with $\Omega = 0.1$, *Re* = 2,000.

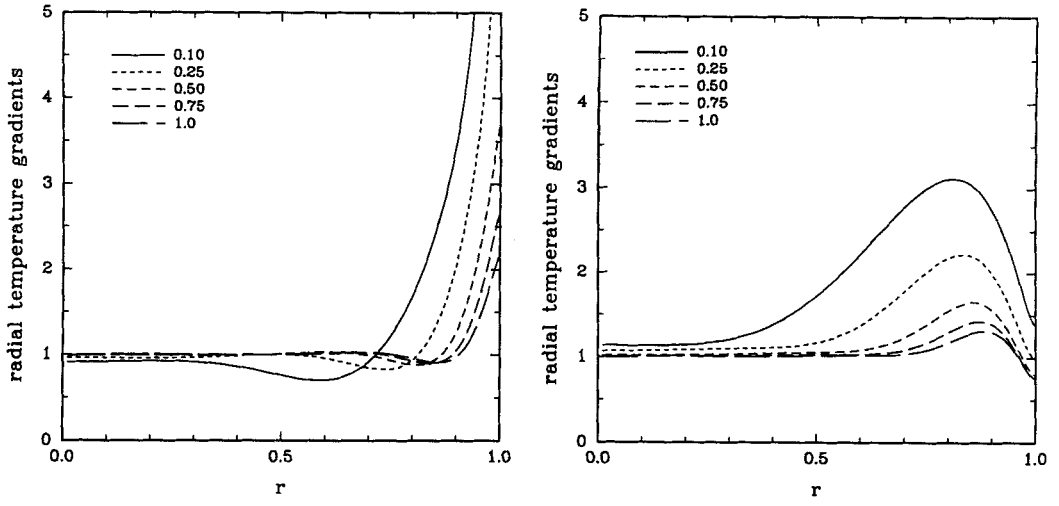

a. At Cold Wall *b. At Hot Wall*

Figure 7. Radial variations of axial temperature gradients for various values of Ω for equal end-rod corotation, *Re* = 2,000.

flow being flattened against the meniscus. In addition, a relatively weaker second cell, with the flow counter to the primary cell, is discernible in the interior of the zone. The effect of the rotation on the temperature profiles within the zone is also significant. As seen in Figure 6, the temperature contours in the interior of the zone correspond closely to the linear conduction profile. In addition, the magnitude of temperature gradients that occur near the meniscus-cold wall boundary are reduced by the end-rod rotation. The reason for this can be ascertained from the contours of the azimuthal velocity in Figure 6, which indicate that the flow in the interior of the zone is in a state of rigid rotation with the end rods. Thus heat transport across the streamlines of this azimuthal flow can take place only through conduction. The nature of the streamlines and the temperature profile in the interior of the zone also indicates that convective

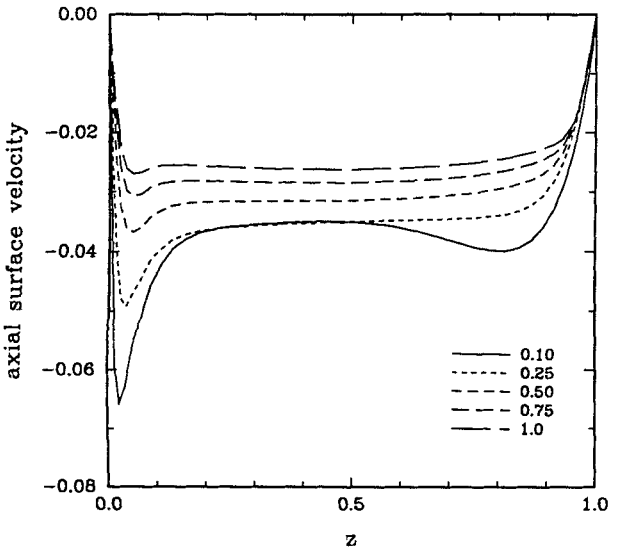

Figure 8. Surface velocity as a function of axial coordinate for various values of Ω for equal end-rod corotation, *Re* = 2,000.

effects in the regions close to the meniscus do not significantly influence or alter the behavior in the interior regions. A similar conclusion was reached analytically by Smith (1986) in the more restricted context discussed earlier.

The axial temperature gradients at the end rods are shown in Figure 7. These gradients are seen to become more uniform over the cross section of the zone as the rotational velocity is increased. As noted earlier, this is a useful property for crystal growth processing. The surface velocities, plotted in Figure 8, are seen to decrease uniformly over the entire extent of the surface as the rotational velocity is increased. This suggests that the heat transport due to convection is also reduced in the boundary layer. This behavior is confirmed by noting that the Nusselt number Nu, shown in Table 2, tends toward the pure conduction value of 0.5 as the rotational velocity is increased.

The confinement and attenuation of the thermocapillary flow due to a uniform corotation of the end rods can be explained in terms of the Taylor-Proudman effect, which constrains the variations in the velocity parallel to the axis of rotation in the slow, steady motions of an inviscid rotating fluid (Greenspan, 1969). The numerical results indicate that the range of validity of the Taylor-Proudman effect is confined to a region near the zone axis at low rotational velocities. Increasing the rotational velocity causes this region to expand outward to the meniscus, shrinking the domain of the viscous Ekman layers at the meniscus in

Table 2. Nusselt Numbers and Minimum, Maximum Values of Axisymmetric Stream Function for Meridional Flow as a Function of End-Rod Angular Velocity*

Ω	Nu_1	Nu_2	$-\Psi_{min} \times 10^3$	$\Psi_{max} \times 10^3$
0.0	−1.721	1.708	3.58	0.00
0.1	−1.121	1.111	1.56	0.14
0.25	−0.786	0.784	1.03	0.16
0.5	−0.618	0.617	0.70	0.14
0.75	−0.564	0.563	0.54	0.12
1.0	−0.540	0.540	0.45	0.11

*Top and bottom end rods are corotated (s = 1); Re = 2,000

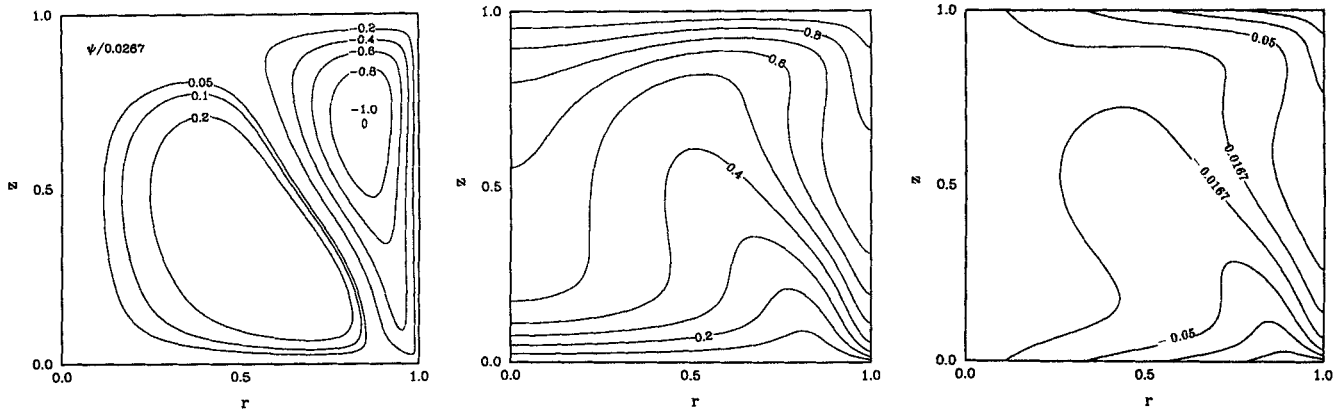

a. Streamlines of Meridional Flows *b. Temperature Contours* *c. Equally Spaced Angular Velocity Contours*

Figure 9. Equal end-rod counterrotation with Ω = 0.15, *Re* = 2,000.

which the thermocapillary layers are confined. The present results indicate that the linear boundary layer analysis of Smith (1986) provides a good qualitative picture of the nature of the flow in a uniformly rotated zone even under moderately nonlinear conditions.

Counterrotated end rods, Ω ≠ 0, s = −1

Harriott and Brown (1983) have shown that in the absence of thermocapillary effects the flow in the counterrotated configuration at low rotational velocities consists primarily of an azimuthal shear. The axial variations of the centripetal pressure due to the primary flow generates a secondary meridionial flow through inertial coupling. These meridional flows comprise two vertically stacked cells in which the fluid circulates toward the axis in the middle of the zone and toward the meniscus in the region near the end rods. These rotationally driven flows can play an important role in modifying the characteristics of the basic thermocapillary flow discussed earlier in this paper.

The streamlines of the meridional flow plotted in Figure 9 show that the thermocapillary cell is pushed toward the meniscus-hot wall corner by the appearance of the analog of one of the rotationally driven flow cells near the cold wall. The analog of the other rotationally driven flow cell cannot be perceived here since its circulation is in the same direction as the thermocapillary flow cell. From the results in Table 3, it is seen that the strength of the circulation in the lower cell increases with the rotational velocity. The strength of the circulation in the upper cell initially decreases but eventually also shows an increase with the rotational velocity. This can be explained by noting that the direction of the flow in the lower cell near the meniscus opposes the thermocapillary flow, which is directed along the surface from the hot wall to the cold wall. This flow collision decreases the surface axial temperature gradients that are responsible for the primary thermocapillary flow in the upper cell. At larger rotational velocities this decrease is offset by the increasing influence of the analog of the upper rotationally driven cell, which also reestablishes the surface temperature gradients that drive the thermocapillary flow. These two effects taken together lead to the eventual increase in the strength of the circulation of the upper cell.

The axial velocity profiles at the meniscus surface in Figure 10 show that the magnitude of the relative maximum near the hot surface first decreases and eventually increases with the rotational velocity in a manner consistent with the discussion given above. Additional confirmation is provided by the axial temperature profiles at the surface in Figure 11, which show the initial decrease and the eventual increase in the temperature gradient in the interior portion of the surface as the rotational velocity is increased. The influence of the end-rod counterrotation on the local heat transfer at the cold wall is also significant. At low rotational velocities the dominant contribution to the

Table 3. Nusselt Numbers and Minimum, Maximum Values of Axisymmetric Stream Function for Meridional Flow as a Function of End-rod Angular Velocity*

Ω	Nu_1	Nu_2	$\Psi_{min} \times 10^3$	$\Psi_{max} \times 10^3$
0.0	−1.721	1.708	3.58	0.00
0.05	−1.505	1.493	2.80	0.13
0.15	−1.607	1.600	2.68	1.35
0.25	−1.873	1.862	3.39	2.13
0.35	−2.123	2.101	3.77	2.65

*Top and bottom end rods are counterrotated ($s = -1$); $Re = 2{,}000$

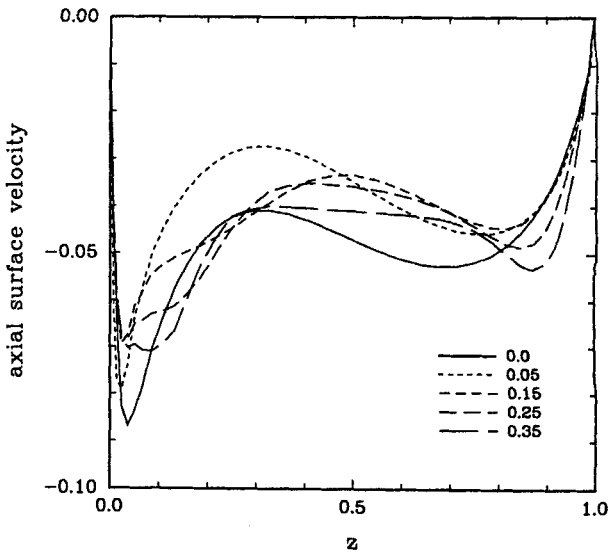

Figure 10. Surface velocity as a function of axial coordinate for various values of Ω for equal end-rod counterrotation, *Re* = 2,000.

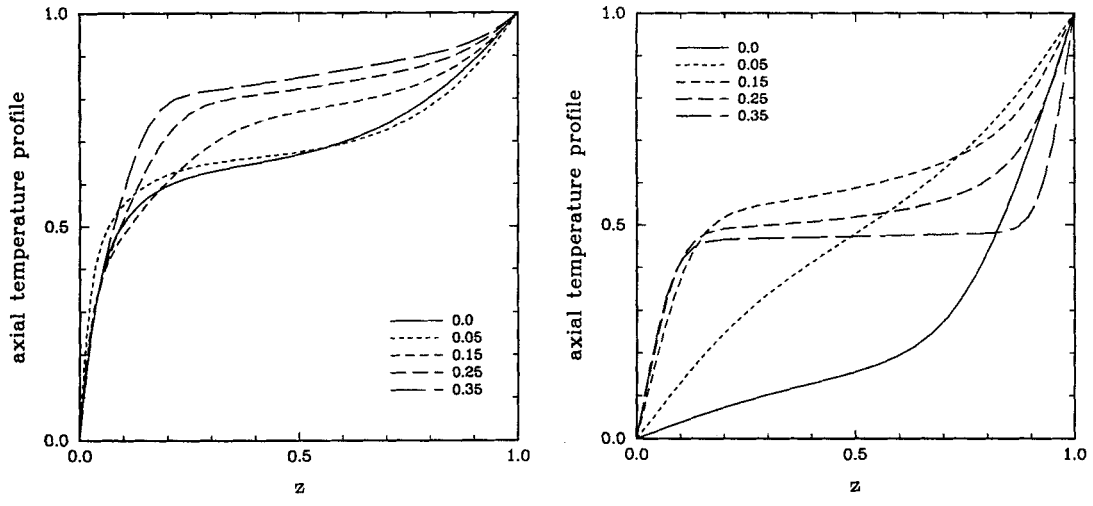

a. At Surface *b. At Zone Axis*

Figure 11. Axial temperature profiles for various values of Ω for equal end-rod counterrotation, *Re* = 2,000.

heat transfer comes from the sharp gradients in the vicinity of the meniscus-cold wall corner. At larger rotational velocities the flow in the lower cell is effective in transporting heat from the warmer upper cell to the regions near the zone axis. As a result, the local minimum in the heat transfer rate shifts away from the axis of the zone toward the meniscus, as shown in Figure 12. Although the largest local heat transfer rates still arise from the primarily thermocapillary flow effects near the meniscus-cold wall boundary, the contribution of the interior regions to the overall Nusselt number *Nu* grows with increasing rotational velocity.

Conclusions

The results presented here deal with the characteristics of thermocapillary flows in a float zone under microgravity conditions and with the modifying effects of various end-rod rotation strategies. Solutions to the field equations are obtained by a Galerkin finite-element discretization coupled with Newton's method to solve the resulting set of nonlinear algebraic equations. The influence of an equal corotation and an equal counterrotation of the end rods on the structure of the flow and temperature fields in the zone was examined. The corotation strategy leads to a confinement of the thermocapillary flows near the meniscus, thereby giving rise to more uniform thermal conditions in the bulk of the zone. The counterrotation strategy leads to stronger flows in the interior of the zone. This may be advantageous in situations where it is desired to promote the vigorous lateral mixing of a solute additive in the melt phase. This, for example, is often the case in semiconductor manufacturing technologies, where the float zone process is carried out in order to incorporate a dopant into a homogenous crystalline material.

Acknowledgment

Computer time was provided through the MIT local allocation at the John von Neumann Center at Princeton, New Jersey, which is supported by the National Science Foundation. The author thanks R. A. Brown (MIT) for useful conversations.

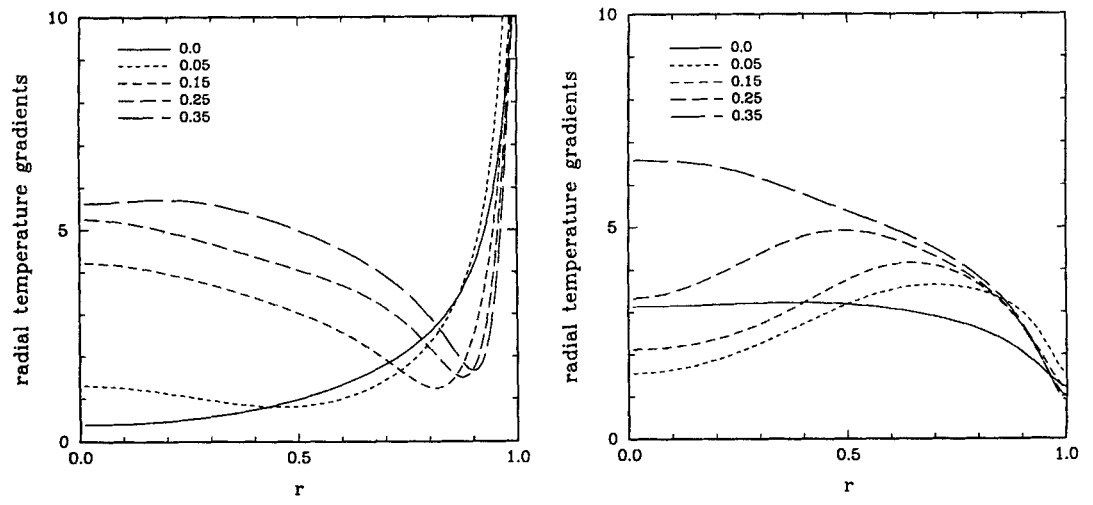

a. At Cold Wall *b. At Hot Wall*

Figure 12. Radial variations of axial temperature gradients for various values of Ω for equal end-rod counterrotation, *Re* = 2,000.

Literature Cited

Carruthers, J. R., and L. R. Testardi, "Materials Processing in the Reduced Gravity Environment of Space," *Ann. Rev. Mater. Sci.*, **13,** 247 (1983).

Chun, C. H., "Marangoni Convection in a Floating Zone Under Reduced Gravity," *J. Crys. Growth*, **48,** 600 (1980).

Chun, C. H., and W. Wuest, "Suppression of Temperature Oscillations of Thermal Marangoni Convection in a Floating Zone by Superimposing of Rotating Flows," *Acta Astronautica*, **9,** 225 (1982).

Fowlis, W. W., and D. O. Roberts, "Confinement of Thermocapillary Floating-zone Flow," *J. Crys. Growth*, **74,** 301 (1986).

Greenspan, H. P., *The Theory of Rotating Fluids*, Cambridge U. Press (1969).

Harriott, G. M., and R. A. Brown, "Flow in a Differentially Rotated Cylindrical Drop at Low Reynolds Number," *J. Fluid Mech.*, **126,** 269 (1983).

———, "Flow in a Differentially Rotated Cylindrical Drop at Moderate Reynolds Number," *J. Fluid Mech.*, **144,** 403 (1984).

Hood, P., "Frontal Solution Program for Unsymmetric Matrices," *Int. J. Num. Meth. Eng.*, **10,** 379 (1976).

Kim, K. M., and A. F. Witt, and H. C. Gatos, "Crystal Growth from the Melt Under Destabilizing Gradients," *J. Electrochem. Soc.*, **119,** 1218 (1972).

Kobayashi,, N., "Computer Simulation of the Steady Flow in a Cylindrical Float Zone Under Low Gravity," *J. Crys. Growth*, **66,** 63 (1984).

Kobayashi, N., and W. R. Wilcox, "Computational Studies of Convection Due to Rotation in a Cylindrical Float Zone," *J Crys. Growth*, **59,** 616 (1982).

Murthy, J. Y., "A Numerical Simulation of Flow, Heat and Mass Transfer in a Floating Zone at High Rotational Reynolds Numbers," *J Crys. Growth*, **83,** 23 (1987).

Priesser, F., D. Schwabe, and A. Scharmann, "Steady and Oscillatory Thermocapillary Convection in Liquid Columns with a Free Cylindrical Surface," *J. Fluid Mech.*, **126,** 545 (1983).

Rybicki, A., and J. M. Floryan, "Thermocapillary Effects in Liquid Bridges. I. Thermocapillary Convection," *Phys. Fluids*, **30,** 1956 (1987).

Smith, M. K., "Thermocapillary and Centrifugal-Buoyancy-Driven Motion in Rapidly Rotating Cylinder," *J. Fluid Mech.*, **166,** 245 (1986).

Thomasset, F., *Implementation of Finite Element Methods for Navier-Stokes Equations*, Springer (1981).

Zebib, A. G., G. M. Homsy, and E. Meiburg, "High Marangoni Number Convection in a Square Cavity," *Phys. Fluids*, **28,** 3467, (1985).

Manuscript received Apr. 8, 1988, and revision received Nov. 18, 1988.